doi:10.1016/S0022-2836(03)00583-7 J. Mol. Biol. (2003) 330, 785–797

JMB

Available online at www.sciencedirect.com

SCIENCE DIRECT®

# Hierarchical Assembly of $\beta_2$-Microglobulin Amyloid *In Vitro* Revealed by Atomic Force Microscopy

**Neil M. Kad[1,2], Sarah L. Myers[1,3], David P. Smith[1], D. Alastair Smith[3] Sheena E. Radford[1] and Neil H. Thomson[3]***

[1]*School of Biochemistry and Molecular Biology, University of Leeds, Leeds LS2 9JT, UK*

[2]*Department of Molecular Physiology and Biophysics, 115 Health Science Research Facility, University of Vermont Burlington VT 05401, USA*

[3]*Department of Physics and Astronomy, University of Leeds E. C. Stoner Building, Leeds LS2 9JT, UK*

**Corresponding author*

The kinetics of spontaneous assembly of amyloid fibrils of wild-type $\beta_2$-microglobulin ($\beta_2$M) *in vitro*, under acid conditions (pH 2.5) and low ionic strength, has been followed using thioflavin-T (ThT) binding. In parallel experiments, the morphology of the different fibrillar species present at different time-points during the growth process were characterised using tapping-mode atomic force microscopy (TM-AFM) in air and negative stain electron microscopy (EM). The thioflavin-T assay shows a characteristic lag phase during which the nucleation of fibrils occurs before a rapid growth in fibril density. The volume of fibrils deposited on mica measured from TM-AFM images at each time-point correlates well with the fluorescence data. TM-AFM and negative-stain EM revealed the presence of various kinds of protein aggregates in the lag phase that disappear concomitantly with a rise in the density of amyloid fibrils, suggesting that these aggregates precede fibril growth and may act as nucleation sites. Three distinct morphologies of mature amyloid fibrils were observed within a single growth experiment, as observed previously for the wild-type protein and the variant N17D. Additional supercoiled morphologies of the lower-order fibrils were observed. Comparative height analysis from the TM-AFM data allows each of the mature fibril types and single protofilaments to be identified unambiguously, and reveals that the assembly occurs *via* a hierarchy of morphological states.



*Keywords:* β2-microglobulin; thioflavin-T; atomic force microscopy; nucleation; assembly mechanism

## Introduction

Amyloidosis is the generic term for the assembly of peptides and proteins *in vivo* into fibrillar aggregates with a common cross-β structure. These aggregates are associated with many debilitating disorders, including Alzheimer's disease, the transmissible spongiform encephalopathies and dialysis-related amyloidosis.[1,2] The onset of aggregation is thought to be initiated by the population of one or more unfolded or partially folded states that are assembly competent.[3] Given the right conditions *in vivo* or *in vitro*, a wide variety of proteins and peptides will self-assemble into amyloid fibrils.[2,4] These fibrils can be detected through the binding of dyes such as Congo red[5] or thioflavin-T (ThT).[6] All amyloid fibrils are characterised by a central core structure of extended cross-β sheet, which can be detected using X-ray fibre diffraction.[7,8] Despite possessing a common cross-β core, amyloid fibrils generated both *in vivo* and *in vitro* have a range of morphologies, which differ in their superhelical twists and the number and arrangement of the associating protofilaments.[9–13] Fully assembled amyloid fibrils can contain different numbers of protofilaments either intertwined into helices or bound side-to-side in a twisted ribbon structure.[9,12,14,15] The final amyloid fibrils often arise through the twisting together of protofibrils, with possible structural rearrangements, to form the consistuent protofilaments.[4] Typical protofibrils, such as those for Aβ 1-42 and Aβ 1-40, are able to bind ThT, but are shorter, have a smaller persistence

N.M.K. & S.L.M. contributed equally to this work.

Abbreviations used: ThT, thioflavin-T; $\beta_2$M, $\beta_2$-microglobulin; TM-AFM, tapping-mode atomic force microscopy; EM, electron microscopy.

E-mail address of the corresponding author: n.h.thomson@leeds.ac.uk

 

length and shorter repeat periods (typically between 20 nm and 30 nm) than their fully assembled fibrillar counterparts.[9,16]

Dialysis-related amyloidosis[17] involves the deposition of predominantly full-length, wild-type $\beta_2$-microglobulin ($\beta_2$M) into amyloid fibrils with structural and tinctorial properties typical of amyloid.[18,19] $\beta_2$M amyloid is typically deposited in collagen-rich tissues, such as cartilage,[20] resulting in carpel tunnel syndrome and pathological bone destruction, and occurs in all patients undergoing long-term renal dialysis.[21] $\beta_2$M forms the non-covalently bound light-chain of the antigen class I HLA complex presented on the cell surface. As part of its normal catabolic cycle, $\beta_2$M is shed from the cell surface, whereupon it is transported in the plasma to the kidneys, which are the major site of degradation of the protein.[22] As a consequence of renal failure, the concentration of full-length wild-type $\beta_2$M in the serum is raised up to 50-fold, thereby initiating amyloidosis *in vivo* by a mechanism currently unknown. *In vitro*, however, a high concentration of $\beta_2$M at neutral pH is not sufficient to initiate formation of amyloid fibrils *de novo*.[23–25] Elongation of seeds from *ex vivo* $\beta_2$M amyloid fibrils is possible *in vitro* at pH 7.4 and is attributed to the existence of a partially folded conformer that is in equilibrium with the native monomer, populated to ~15%.[26,27] Fibril formation at neutral pH can be induced by the addition of $Cu^{2+}$,[28] by cleavage of the N-terminal six residues,[29] or by concentrating and drying of the protein on a dialysis membrane surface.[30]

$\beta_2$M belongs to the immunoglobulin superfamily and has a β-sandwich structure stabilised by a single disulphide bond that is typical of this family of proteins.[31] Under acidic conditions (below pH 5.0) at an ionic strength of 400 mM, $\beta_2$M rapidly and spontaneously forms amyloid fibrils that bind ThT and Congo red, which gives rise to green birefringence, and results in an X-ray diffraction pattern consistent with a cross-β structure.[25] Under these conditions, the native protein is destabilised relative to a partially folded state that retains significant β-sheet secondary structure.[25,32] The fibrils formed under these conditions are short (<600 nm), flexible,[25] have a periodicity of about 30 nm, and are ~3.5 nm high as measured by tapping-mode atomic force microscopy (TM-AFM) in air.[33] Although these fibrils have morphological properties akin to protofibrils seen in other amyloid proteins,[9,34] there is no evidence that they assemble further into long, straight fibrils and therefore they are not defined as protofibrils.[33,35] By contrast, at lower pH (<3) and at low ionic strengths (<30 mM), $\beta_2$M assembles slowly, in a nucleation-dependent manner[24], to form long, straight fibrils that give rise to a cross-beta X-ray fibre diffraction pattern (D.P.S., S. Jones, L.C. Serpell & S.E.R., unpublished results) and have a variety of morphologies including straight aperiodic fibrils, as well as fibrils displaying a left-handed twist with regular periodicity of about 90 nm.[33]

AFM has been used to investigate the higher-order structure of amyloid fibrils formed from a number of peptides and proteins, including Aβ,[9,16,34,36] amylin,[37] immunoglobulin light chain domains,[11] α-synuclein[38,39] and lysozyme,[15] and the protein fibrils formed by the yeast prions Sup35[40,41] and Ure2p.[42] These studies have involved the imaging of samples dried onto mica and other surfaces,[43] as well as *in situ* imaging of fibril growth in real-time under aqueous fluid.[37,44] Whilst imaging of fibril growth in real time can provide information about the polarity of fibril growth and growth kinetics at surfaces, imaging of dried samples can provide detailed information about the distribution of fibril types within a single heterogeneous growth solution, distinguished by their average height, periodicity and helicity. Here, we use TM-AFM in air, in conjunction with negative stain electron microscopy (EM) and the fluorescence of ThT, to examine the events that occur during the growth of amyloid fibrils from monomeric human $\beta_2$M *in vitro* at pH 2.5, 37 °C at low ionic strength. Under these conditions, assembly of $\beta_2$M into amyloid-like fibrils is rapid,[45] results in the formation of long, straight amyloid fibrils with different morphologies,[33] and the assembly mechanism is relatively independent of growth-rate (see below). These conditions are thus ideal for the experiments described. We identify various aggregation events occurring in the lag phase, as well as the emergence of a protofilament species, previously unobserved in studies of the end-points of assembly.[33] The timing of the emergence of higher-order fibrils allows us to propose a hierarchical assembly scheme.

## Results and Discussion

### $\beta_2$M amyloid fibril morphology depends on growth conditions

Representative TM-AFM images of different fibrillar types of human $\beta_2$M formed *ab initio*, *in vitro* under two different conditions at the end-point of growth are shown in Figure 1. Consistent with previous results,[25,33] the fibrils formed at pH 3.6 in 0.4 M NaCl are short (<600 nm), flexible, exhibit a nodular morphology with a repeat distance of about 30 nm, and are ~3.5 nm high (Figure 1(a)). Here, we classify these fibrils as type A. By contrast, fibrils formed at pH 2.5 at low ionic strengths (<30 mM) are long and straight, and display a number of different morphological types, termed here type I (Figure 1(b)); type II (Figure 1(c)) and type III (Figure 1(d)). Consistent with our previous EM and AFM data,[33] these AFM images show clearly that type I fibrils are formed from two intertwined protofilaments and, under these conditions, have a helical repeat of ~60 nm. Type II fibrils, which have not been identified unambiguously before by AFM, are a four protofilament helix formed by the twisting

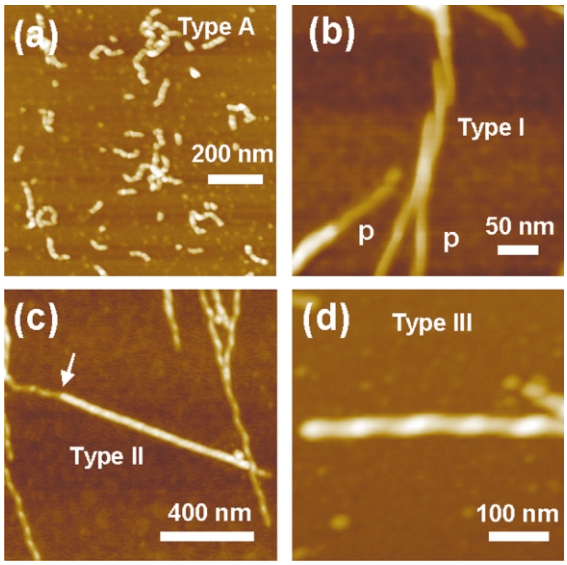


**Figure 1**. TM-AFM images taken in air of different end-point morphologies of hydrated $\beta_2$M amyloid fibrils grown *in vitro* adsorbed onto mica. (a) Type A fibrils grown at pH 3.6 in 0.4 M NaCl at 37 °C. The fibrils in (b)–(d) are all end-point morphologies of fibrils grown at pH 2.5 with no added NaCl at 37 °C. (b) Type I fibrils are formed by the intertwining of two protofilaments (marked p) into a left-handed helix. (c) Type II fibrils are formed from the intertwining of four protofilaments into a helix. The height of the fibril changes from 5 nm to 8.5 nm where a type I fibril protrudes, marked by the arrow. The other fibrils in the image are type I with a supercoiled morphology, which have a superhelical period of 60 nm (see Figure 6), although the consistuent protofibrils cannot be resolved under these imaging conditions. (d) Type III fibrils formed through the lateral association of four protofilaments have a helical repeat of about 100 nm. The false-colour height scales for (a)–(d) are 10, 30, 36 and 50 nm, respectively.

together of two type I fibrils and have a repeat period of 60 nm in this case. A shorter axial period of 30 nm was detected in the TM-AFM amplitude signal. These two periods are consistent with two type I fibrils with a helical repeat of 60 nm supercoiled around each other. The individual type I fibrils present in Figure 1(c) have a supercoiling period of 60 nm, which is coincident with their axial twisting repeat period (see below). Type III fibrils have a twisted-ribbon morphology, are formed from four protofilaments that are associated laterally, and have rather regular axial repeats, about 70 nm in this case (Figure 1(d)). These fibril types are fully consistent with previously published lower-magnification images of $\beta_2$M fibrils and show that the fibrils grown at low ionic strength have a left-handed helicity.[33]

## Time-courses of $\beta_2$M fibril formation

To determine whether the diverse number of final fibril structures observed in low pH, low ionic strength conditions arises in a temporally parallel or sequential manner and to identify and characterise any intermediate species in the aggregation pathway, fibril formation from monomeric $\beta_2$M was followed in real-time using continuous monitoring of the fluorescence signal from ThT, and *via* a discontinuous assay in which samples were withdrawn at different time-points and imaged by TM-AFM and negative stain EM (see Figures 2–4). Here, we present two kinds of experiment: the first is a comparatively low-time-resolution experiment that follows the overall aggregate density in the lag and demonstrates the timing of the emergence of fibrillar species (Figures 2 and 3). The second experiment is at a higher time-resolution and investigates the nucleation process in more detail (Figure 4). Both experiments were performed at pH 2.5 at low ionic strength (17.4 mM), and a protein concentration of 1 mg/ml. The experiments were performed with 1 ml and 3 ml volume of solution in the fluorimeter cuvette, respectively. This results in differences in agitation efficiencies, which alters the rate of fibril formation (the length of the lag using an identical experimental set-up is reproducible within a standard deviation of 6%). Analysis of the two kinds of experiment using TM-AFM and EM showed no difference in the types of fibrillar and pre-fibrillar species formed, nor of their order of appearance (see below). To facilitate comparison of the results from different experiments, therefore, the time-course of assembly was normalised to the total

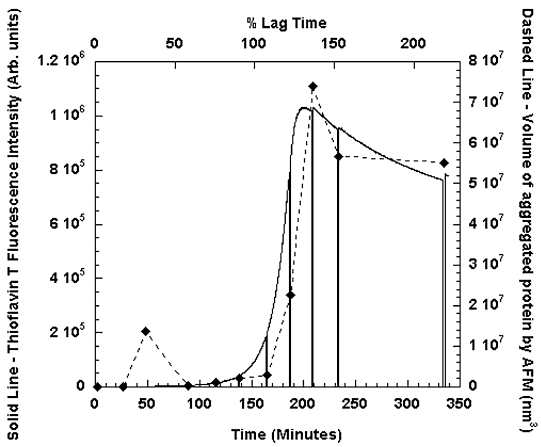


**Figure 2**. $\beta_2$M amyloid growth curve monitored by fluorescence and AFM. Continuous curve, continuous time-course of ThT fluorescence. Each time the ThT signal dropped to zero, an aliquot was taken from the fluorimeter for analysis by AFM and EM. Broken line + diamonds, discontinuous assay of the volume of aggregated protein (amorphous or fibrillar) bound to the mica surfaces as measured by TM-AFM of air-dried samples. The error bars are the standard errors taken from the average of the total volume on the surface from four or five, 5 μm × 5 μm areas at each time-point. The percentage surface area covered by the aggregated protein was calculated from the AFM images and it gave the same shape curve as the volume (data not shown).

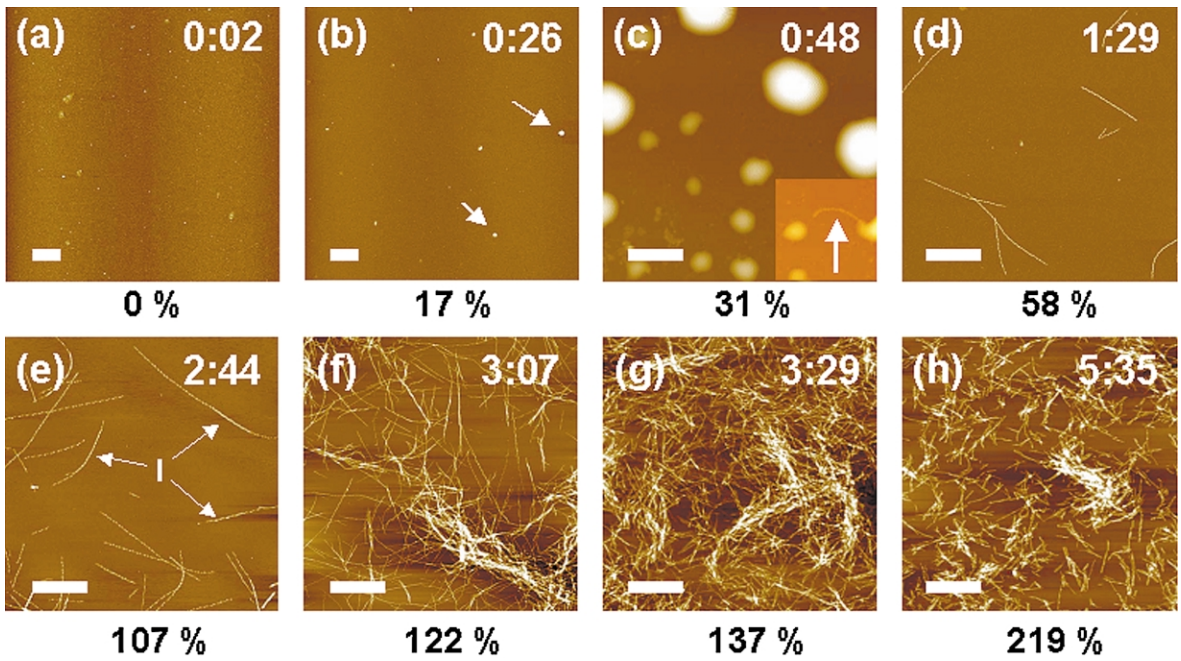


**Figure 3**. Low-magnification, TM-AFM images in air of aliquots deposited onto mica taken from different time-points assayed during the growth of $\beta_2$M fibrils. The time after growth was initiated is shown in the top right-hand corner of each image (hours:minutes). The percentage of the total lag time passed is shown below each image. The definition used for the lag time is described in Materials and Methods, and in this experiment it is 153($\pm$1) minutes. (a) After two minutes the solution is monodisperse and comprises $\beta_2$M monomers. Density fluctuations in the protein solution cause amorphous aggregates to form ((b) and (c)), which disappear with a concomitant rise in fibril density ((d)–(h)). The arrows in (b) indicate aggregates present after 26 minutes. (c) By 48 minutes, the number and size of aggregates observed have increased. The arrow in (c) marks a fibril that appears to protrude from one of the aggregates. The contrast of the image in this corner was optimised to show the fibril, which is much lower in height than the aggregates. Estimates indicate that the aggregates in (b) and (c) contain $10^2$–$10^4$ monomers and $10^3$–$10^6$ monomers, respectively. These estimates should be taken as upper limits, since the hydration state of the aggregates is not known. (d) After the disappearance of the amorphous aggregates, individual protofilaments are observed. Their formation precedes development of the higher-order type I, II and, finally, type III fibrils. After two hours and 44 minutes the lag time is over and the protofilaments are twisted together to form type I fibrils. Three type I fibrils incorporating two protofilaments are marked in (e) by the arrows. In (d) and (e) all the protofilaments and type I fibrils have a super-coiled morphology (see Figure 5). All scale bars represent 1 μm and the maximum height scales for the false-colour images are 10, 20, 200, 30, 30, 50, 50 and 50 nm, respectively.

length of the observed lag phase (see Materials and Methods).

## Global changes in the aggregating protein solution

Figure 2 shows a typical ThT curve (continuous line) obtained when $\beta_2$M assembles into amyloid-like fibrils at pH 2.5. Under these conditions, $\beta_2$M amyloid forms with nucleation-dependent kinetics typified by a significant lag phase, consistent with previous results for this[1,46,47] and other proteins.[4,48,49] Although the increase in ThT fluorescence indicates that amyloid fibrils have formed, this assay provides no information about the nature of events occurring in the lag-phase or the changes in fibril morphology *versus* time. At judiciously chosen time-points, therefore, aliquots were taken from the aggregating protein solution and deposited onto mica or colloidion-coated EM grids for structural investigation using TM-AFM in air and negative stain EM. Overall, 11 samples, taken approximately every half an hour, were analysed in this manner. Figure 3 shows TM-AFM images obtained at eight representative time-points. During the lag phase there is a small fluorescence signal, during which time nucleation centres for fibril growth are presumably forming. At about 150 minutes, a rapid increase in the ThT signal occurs, presumably because the concentration of nuclei has surpassed a critical concentration.

The volume of aggregated protein present on the mica surface at each time-point in the AFM experiments is plotted in Figure 2 (dotted line). The data show a lag phase with subsequent rapid growth that correlates well with the kinetics observed by ThT fluorescence. The AFM imaging revealed that at early time-points in the lag phase (up to two minutes ($<$1% of the total lag)) the protein solution is essentially monodisperse, forming a smooth layer of protein on the mica surface (RMS roughness of less than 0.5 nm in 10 μm $\times$ 10 μm scans) (Figure 3(a)). The size of the globular fea-

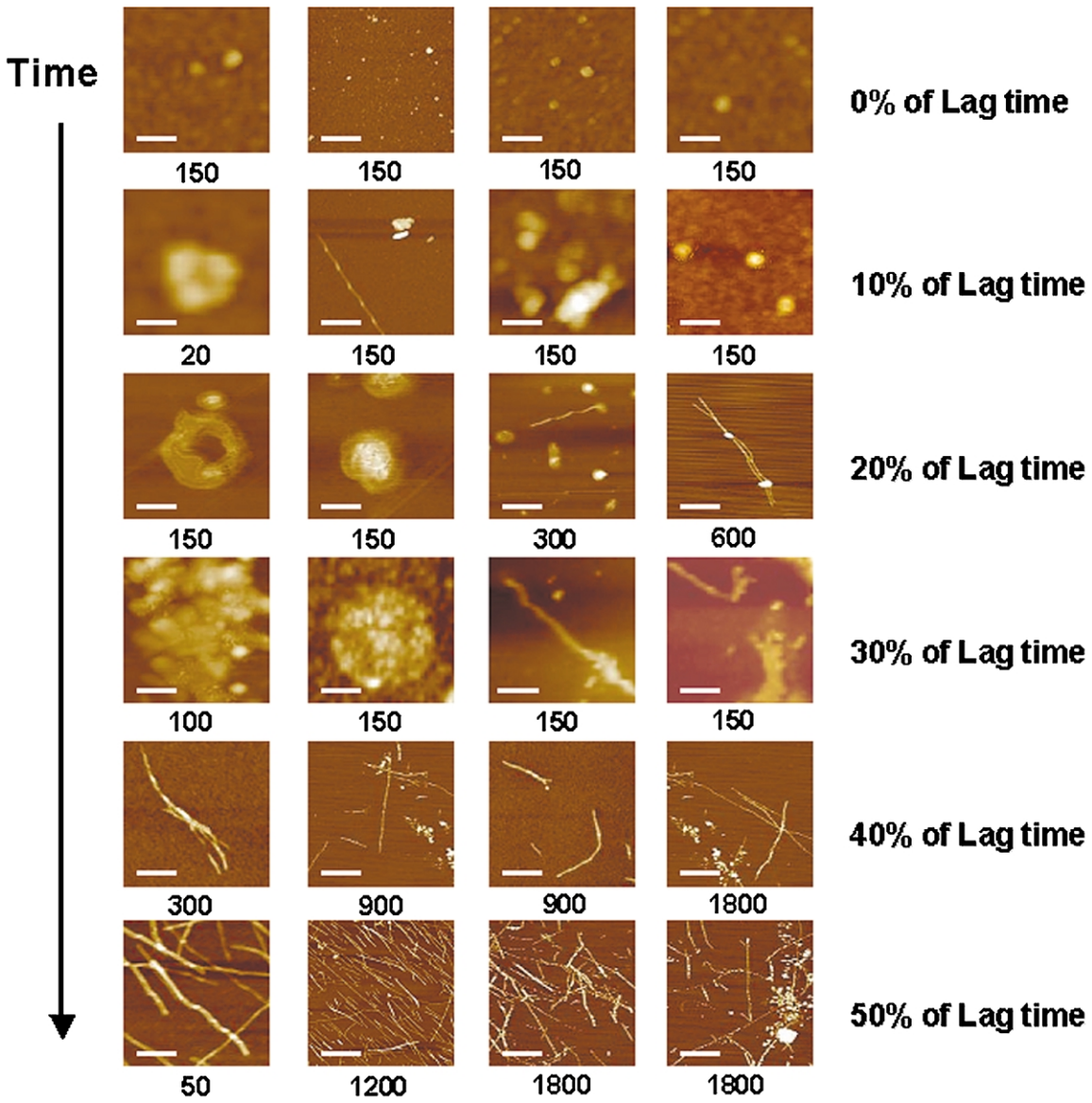


**Figure 4**. Higher time-resolution TM-AFM study of the aggregation process in the lag phase. Samples were taken at intervals of 10% of the overall lag time (this equates to a period of five minutes in this experiment). The images are generally at a higher magnification than Figure 3 and illustrate the diversity of aggregate structures that appear within the nucleation phase. The size (in nanometres) that the scale bar represents is given below each image. The images presented are from two experiments, which both had absolute lag times of 50(±1) minutes. Eight repetitions of the ThT fluorescence experiment for this protein stock gave an average absolute lag time of 52.3(±3.1) minutes.

tures on the surface is 10–12 nm in diameter (data not shown). Taking the broadening of the sample by the AFM tip into account, especially in samples that are not close-packed, these dimensions would be consistent with monomeric protein, or with small oligomeric species (note that the protein is known to be monomeric at time zero).[33] More interestingly, however, larger globular, amorphous protein aggregates are observed at later times in the growth curve (Figure 3(b) and (c)). At 26 minutes after the initiation of aggregation (17% of the total lag time) (Figure 3(b)), the aggregates range in height from 3 nm to 15 nm and full-width from 70 nm to 320 nm. At 48 minutes (~30% of the lag time) (Figure 3(c)), larger aggregates are seen, ranging in height from 3 nm to 85 nm and in full-width from 70 nm to 1300 nm.

The AFM data show that the amorphous aggregates grow rapidly in size and number during the lag phase, as shown by the peak in the volume of deposited aggregated protein that forms a maximum in the growth curve at 48 minutes (Figure 2). These aggregates then disappear before the sharp rise in the volume of amyloid fibrils occurs. The amorphous aggregates do not give rise to a corresponding peak in the fluorescence signal, indicating that they do not bind ThT. Negative stain EM images were taken from aliquots at each time-point. The images correlate well with the low-magnification AFM data, but showed, in addition, a

small number of mature amyloid fibrils at early time-points (within the first 20–30% of the lag time). Consistent with this, high-magnification TM-AFM images of the amorphous aggregates showed occasional fibrillar structures apparently emerging from their centres (Figure 3(c)). In these experiments, therefore, amyloid formation occurs through protein density fluctuations, which slowly cause formation of amorphous aggregates that could contain the nucleation centres for fibril growth.

At later time-points during assembly (>48 minutes/30% of the lag), amorphous aggregates were no longer observed by TM-AFM (Figure 3(d)–(f)) or EM (data not shown). The increase in fibril density on the mica samples monitored by AFM over this time-scale occurs concomitantly with the increase in the ThT fluorescence (Figure 2) and is caused by the formation of fibrils composed of only a single filament (Figure 3(d)). At later times, more highly assembled fibrils emerge. These comprise two or four protofilaments and are identical with the fully assembled type I, II and III fibrils shown in Figure 1. All the single-filament fibrils shown in Figure 3(d) are indistinguishable from the protofilaments that compose the fully assembled fibrils, although they have a zig-zag appearance that arises from supercoiling (see below). These single filaments have no internal structure resolvable by TM-AFM. Since the individual filaments are indistinguishable from the constituent protofilaments of fully assembled fibrils, they could be classed as protofibrils. However, their morphology is very different from the protofibrils identified in the assembly of Aβ 1-40 and Aβ 1-42.[9,16] Interestingly, no type A fibril was observed during the growth assays, despite surveying a large number of samples from several repeat experiments using both TM-AFM and EM. These observations confirm previous results,[33] that type A fibrils are not protofibrils, but are the end-product of an independent assembly mechanism.

The ThT signal in Figure 2 reaches a maximum at three hours and 20 minutes, and then decreases. There are two reasons for this. Firstly, the fibril density is high at this time, increasing light-scattering. Secondly, aggregated fibrils were seen precipitating from solution after this time, which reduces the fluorescence intensity. Consistent with this, the AFM data show a correlated decrease in fibril density on the mica surface (cf. Figure 3(g) and (h)). The average length of the fibrils on the mica decreases at later time-points (see Figure 3(h)), supporting the view that the longer fibrils aggregate more readily and precipitate out of solution.

### Amorphous aggregates with a variety of morphologies form in the lag phase

Figure 4 shows a summary of TM-AFM data obtained from a fibril assembly curve obtained at higher-time-resolution than that shown in Figures 2 and 3. In this experiment, time-points were obtained every five minutes during the lag time, as well as at later time-points during assembly. TM-AFM images were obtained from several replicate experiments, each had a similar lag time of 52.3(±3.1) minutes ($n = 8$). As shown in Figure 4, amorphous aggregates form early in the lag phase of assembly, consistent with the results shown in Figures 2 and 3. More detailed analysis of the species formed early during the lag phase, however, revealed a variety of different aggregated forms, including pore-like structures, larger toroidal rings and more globular species, akin to species observed in the lag time of assembly for a variety of other proteins.[34,50–55] The images shown in Figure 4 are representative of the most commonly observed species that were observed in all growth curves examined to date. We cannot rule out, however, the possibility that other morphologically distinct species might form during assembly that have not been detected. The role of the different species in the assembly mechanism cannot be deduced from the discontinuous assay performed. Nonetheless, the data show clearly that the first species to form in the lag time are small globular or pore-like structures. These are then replaced with larger aggregates that are maximally populated at 30% into the lag phase. Thereafter, increasing numbers of fibrils appear and little amorphous aggregate remains (see the 40% time-point in Figure 4). The experiment shows that a small number of fibrils are present at early time-points, often in conjunction with amorphous aggregates (see the right-hand image at the 20% time-point in Figure 4). The transition from aggregate to fibril appears to be rapid, occurring in less than 10% of the overall lag time and reproducibly between 30% and 40% of the total lag time. Further experiments, possibly using real time growth studies in solution, will be needed to determine the role, if any, of each of these species in nucleating the assembly of protofilaments and higher-order fibril assemblies with different morphologies.

### Growth conditions can induce a super-helical morphology in protofilaments and type I fibrils

Protofilaments and type I fibrils formed in these experiments showed a superhelical morphology caused by a supercoiling over and above the intertwining of protofilaments. These morphologies were not observed in our previous study,[33] possibly because of the different agitation conditions used. Figure 5(a) and (b) shows TM-AFM and EM images of type I fibrils with well-defined superhelical repeats. These fibrils have a zig-zag appearance caused by a flattening of the toroidal superhelix onto a flat surface during sample preparation. The superhelical repeats range between 60 nm and 150 nm, and for the type I fibrils this repeat is often coincident with the helical repeat so that there are two axial twists per superhelical period, as is the case for the examples shown in Figure 5. It is not possible to distinguish by AFM the

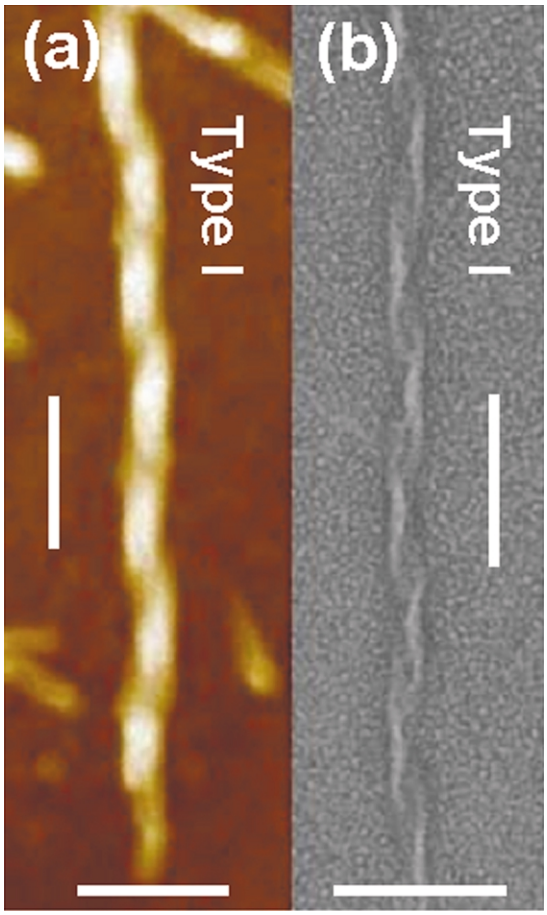


**Figure 5**. The superhelical morphology of type I fibrils. (a) TM-AFM image of a superhelical type I fibril present at 122% lag time. (b) Corresponding negative stain EM image of a superhelical type I fibril present at 69% lag time. In both of these images the super-helical period is coincident with twice the twist period, giving a zig-zag appearance to the fibrils. The axial periods are 145 nm and 130 nm, respectively. The scale bars all represent 100 nm.

handedness of the supercoiling in fibrils flattened into the zig-zag morphology, such as those in Figure 5. However, other supercoiled protofilaments showed exclusively left-handed superhelical periods (see Figure 6(a)). Type II and type III fibrils generally did not exhibit supercoiling, possibly because they are much more rigid than the protofilaments and type I fibrils (as evidenced by their longer persistence lengths).

### $\beta_2$M fibrils assemble in a hierarchical manner

Although TM-AFM in air does not necessarily measure true heights of biomolecules, comparative measurements can be used to identify different species if the imaging parameters are similar. Table 1 summarises the dimensions of different fibril types measured by TM-AFM, including their height, width, helicity, the range of their axial repeat periods, whether they are supercoiled under these growth conditions and the range of the supercoiling repeat distances. Protofilaments and type I and type II fibrils can be distinguished on the basis of their average heights $\langle h \rangle$, together with their different characteristic morphology. Protofilaments have an average height of $4(\pm 1)$ nm, type I fibrils are $5(\pm 1)$ nm high and type II fibrils are $8(\pm 1)$ nm high. Type III fibrils have an average height of $5(\pm 1)$ nm, a consequence of their large aspect ratio in cross-section. The protofilaments and type I fibrils thus have similar average heights, but can be distinguished from each other through their average width along the length of a fibril measured at half the average maximal height $\langle h_{max} \rangle$. Despite being similar in height to type I fibrils, type III fibrils can be distinguished readily from other fibril types, since they have the largest ratio in peak-to-trough height difference of any of the fibrils observed here. Unambiguous identification of each species using the parameters listed in Table 1 allowed the occurrence of different fibrillar species to be followed as the growth progressed. Figure 6 shows a selection of high-magnification negative stain EM and TM-AFM images taken at different times during assembly of the fibrils. The first fibrils observed in the TM-AFM images (~60% into the lag phase) are protofilaments (Figures 3(d), and 6(a) and (b)). These are straight, single filaments in which no sub-filaments have been resolved by either AFM or EM. At later times during the lag phase (~70% into the lag and beyond) type I fibrils appear, the branched morphology at their termini suggesting that they are formed by the inter-twining of two protofilaments that arise by a hierarchical assembly mechanism (Figures 1(b) and 6(d)). Towards the end of the lag phase (65–100% of the lag) protofilaments, type I fibrils and type II fibrils co-exist (Figure 6(d)). This illustrates the hierarchical nature of assembly achieved through intertwining of protofilaments into higher-order structures, and shows that the assembly is very heterogeneous in time with three different fibril types co-existing at late times in the lag phase. Type III fibrils occur at later stages during growth than the lower-order fibrils, and are first observed only when the lag phase is complete (Figure 6(e) and (f)). Once fibril formation has reached steady state, identification of fibril types using both EM and TM-AFM was difficult due to the high density of fibrils on the support surfaces, and the subsequent loss of longer fibrils as a consequence of their precipitation from solution. Whether unassembled protofilaments remained at the later time-points could not be assessed. Nonetheless, the data indicate that $\beta_2$M amyloid fibrils form in a hierarchical manner in which single protofilaments are the first fibrils to form. Similar results have been observed for several other amyloidogenic proteins.[9–11,16] On the basis of our results, two possible mechanisms of fibril formation can be envisaged: (1) the lower-order fibrils essentially form fully first and then associate laterally and intertwine to form higher-order structures; or (2) nucleation centres form in

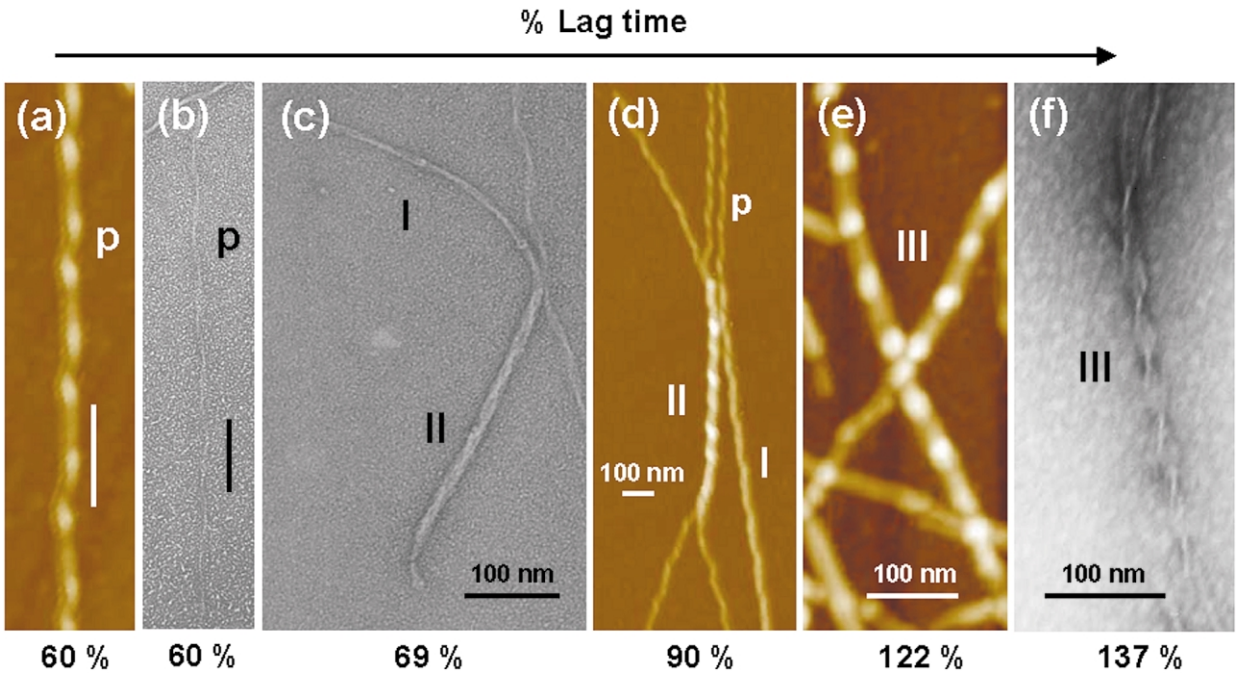


**Figure 6**. A selection of high-magnification TM-AFM and negative stain EM images of different fibril structures formed at increasing times during the assembly of amyloid fibrils from $\beta_2$M. AFM images are in colour and EM images are in grey-scale. (a) TM-AFM image and (b) negative stain EM images of supercoiled protofilaments at 60% lag time. (c) EM image of a type I fibril twisting into a type II fibril. A type I fibril with a superhelical twist lies alongside. (d) TM-AFM image of protofilaments, type I and type II fibrils that co-exist at this stage of assembly. (e) TM-AFM image of a type III fibril formed by lateral assembly of protofilaments with an axial repeat of about 70 nm. (f) Negative stain EM image of a type III fibril with an axial repeat period of about 50 nm.

the lag phase that contain short protofilaments either alone or with two or four protofilaments associated laterally, which then extend *via* monomer extension. Although previous results have suggested that fibrils of $\beta_2$M formed by extension of seeds occurs by monomer addition,[24] which of these possibilities describes the formation of higher order fibrils remains to be determined.

The scheme in Figure 7 summarises the assembly mechanism of $\beta_2$M fibrils determined from this study. Initially, a decrease in pH induces the unfolding of the native monomer and initiates

**Table 1.** Summary of various dimensions and properties of the different $\beta_2$M fibril types

| β2-Microglobulin fibril type | Average height (nm) (of fibril above mica surface) $\langle h \rangle$ | Peak-to-trough heights along backbone of fibril (nm) | Average maximal height of the fibril (nm) $\langle h_{max} \rangle$ | Average width (nm) (measured at half of average maximal height) | Helicity? | Axial repeat periods (nm) | Is it supercoiled under vigorous stirring? | Supercoiling axial repeat period (nm) |
|---|---|---|---|---|---|---|---|---|
| A | 2.2 ± 0.5 | 2–4.5 | 3.3 ± 0.3 | 18 ± 1 | None resolvable | 20–30 | – | – |
| Protofilament | 4 ± 1 | 2–6.5 | 2.9 ± 0.2 | 17 ± 3 | No | – | Yes | 25–60 |
| I | 5 ± 1 | 3.5–6.0 | 4.3 ± 0.3 | 25 ± 4 | Left-handed | 50–80 | Yes | 60–150 |
| II | 8 ± 1 | 6–8.5 | 7.8 ± 0.3 | 33 ± 3 | Left-handed | 30–60 | No | – |
| III | 5 ± 1 | 4–10 | 6.5 ± 0.5 | 32 ± 3 | Left-handed | 40–100 | No | – |

The average fibril height is defined as the mean of the height data histogram above the mica background. This is therefore not necessarily physically the top of the fibril but represents a plane through the fibril at the average vertical height. The errors for these measurements are taken from the standard deviation of the height histograms. The peak-to-trough heights are the range of heights above the mica background for the maxima and minima along the backbone of the fibrils. The average maximal height is the mean of the backbone height along the fibril, i.e. the average of the peak-to-trough variation. The widths are expressed as the mean width measured at half the average maximal height to compensate for the majority of tip-broadening. The errors in this measurement are estimated from the edge slope of the average fibril profile. The axial repeat periods in the absence and in the presence of supercoiling have been expressed as ranges, due to their variability. The data presented with errors are averages and standard deviations of four to six fibril segments ranging between 50 nm and 400 nm long.

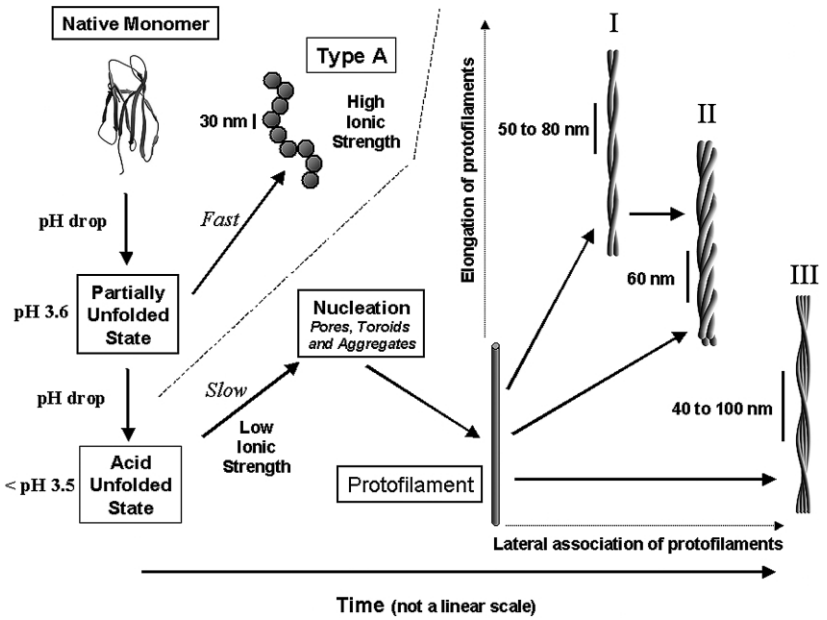


**Figure 7**. A representation of the different amyloid fibril morphologies of $\beta_2$M formed *de novo in vitro*, and their formation pathways. A decrease in pH causes the native monomer to partially unfold. In high-salt conditions this species assembles rapidly into fibrils with a type A morphology.[25,32] A further decrease in pH causes the protein to unfold to the acid-unfolded state.[25,33,54] This species aggregates into various amorphous aggregate structures during the nucleation phase, after which single protofilaments appear. These protofilaments then extend lengthways and assemble laterally to form fibrils with a range of morphologies containing two or four protofilaments, as helices or twisted ribbons. The comparative lengths of the fibril morphologies identified suggest that protofilament extension occurs more rapidly than protofilament side-to-side self-assembly. The arrows indicate which fibrils are related, as evidenced from the protrusion in EM or TM-AFM images of the lower-order fibril from the higher-order one.

fibril formation.[25,33] At a pH of ~3.6, $\beta_2$M is partially unfolded and these species rapidly assemble at high ionic strength into type A fibrils that have a characteristic 30 nm nodular repeat.[25,33] At lower pH values (<pH 3.6), $\beta_2$M forms an acid-unfolded state.[25,33,56] At low ionic strengths, this species assembles *via* nucleation-dependent growth[24,33,45,57] into long, straight fibrils with a range of morphologies. The nucleation event in the conditions studied here is correlated with the formation of various protein aggregates, from which single protofilaments develop. Higher-order fibrillar assemblies then form either by elongation of nuclei, or by the association of preformed protofilaments or a combination of both. We observe generally that as the number of protofilaments in the fibrils increases, the length decreases. Type II and III fibrils have lengths in the range 100–500 nm, whereas the protofilaments and type I fibrils are often longer than this (see Figure 3(d) and (e)). Also, the abundance of the type II and type III fibrils observed and identified is relatively low compared with the number of individual protofilaments and type I fibrils (the former are estimated to comprise less than 5% of the population at the end of the lag phase). These observations suggest that, under the conditions of these experiments, elongation is faster than lateral association. How then do type III fibrils form? Consideration of the topology of these fibrils makes it seem unlikely that these fibrils will form directly from type I or type II fibrils, or that these fibrils form as a consequence of deposition of type I or type II fibrils on the surface, since this would require unwinding or complete rearrangement of their structure. This idea is supported by the fact that branching from type III fibrils has not been observed. It is perhaps more likely that each of these fibrillar types arises from a common nucleation core, which diverges in structure early on during growth.

## Summary and biological implications

Using TM-AFM in air, we have imaged hydrated amyloid fibrils formed at different times during the assembly of $\beta_2$M amyloid fibrils and have characterised them on the basis of their properties, including the average height, the amplitude of the axial repeat and by the observation of the number of their consistuent protofilaments. By monitoring the assembly reaction during continuous growth, we have shown that the three predominant types of fully assembled amyloid fibrils observed previously[33] form in a hierarchical manner. Similar to observations of fibril assembly using other amyloidogenic proteins,[34,37,41,49–53,55,58,59] we show that the nucleation phase of $\beta_2$M fibrillogenesis involves the formation of protein aggregates with a range of morphologies, which are followed by the emergence of protofilaments and higher-order fibrillar assemblies. Further details about the structural properties of these pre-fibrillar species and whether they are directly nucleating or are off-pathway entities, as found for similar species in other proteins,[60 61] remains to be revealed.

The formation of fully assembled fibrils of $\beta_2$M occurs in a hierarchical manner, with the single protofilaments and type I fibrils forming first, whilst type II and III fibrils appear later. Whether these fibrils form in a sequential manner or in parallel by assembly from structurally different nucleating centres remains to be determined. Nonetheless, the data presented here highlight the heterogeneity of $\beta_2$M fibril assembly, even under

carefully controlled conditions *in vitro*. Which, if any, of the fibrillar species observed is involved in the development of the symptoms of dialysis-related amyloid, either by their deposition in collagen-rich regions *per se*, through their possible toxicity,[46,54,60–65] or by their interaction with other cellular components, such as monocytes and macrophages,[47] remains to be seen. Demonstration that the assembly of $\beta_2$M fibrils occurs in a hierarchical manner, together with the ability to identify different fibril types simply and unequivocally by AFM, will form the foundations for future experiments that should help to clarify these points.

## Materials and Methods

### Growth kinetics by thioflavin-T assays

A stock solution of 1 mg/ml of $\beta_2$M in water at pH 7.0 was prepared from purified lyophilised recombinant protein.[25] Growth was initiated by the addition of buffer to reduce the pH rapidly to 2.5. The protein was then incubated at pH 2.5 in 25 mM sodium acetate, 25 mM sodium phosphate containing 10 μM ThT at 37 °C. The stock $\beta_2$M sample was filtered through a 0.2 μm cut-off filter to remove large particles that may act as seeds for fibril growth prior to the addition of buffer. Previous experiments using freshly gel-filtered protein showed identical kinetics profiles as monitored by ThT fluorescence.[33] The formation of amyloid was monitored by following the fluorescence of ThT using a spectrofluorimeter (PTI Quantamaster C-61). Excitation of ThT was at 444 nm and the fluorescence was monitored continuously at 480 nm while the sample was stirred vigorously in the cuvette at 1400 rpm. At chosen time-points, 10 μl aliquots of protein were removed and the sample was deposited immediately onto mica. The length of the lag phase is highly dependent on the experimental conditions; higher concentrations of protein decrease the lag time, as does rapid agitation, whilst no lag is seen at higher pH (>3.5) and elevated ionic strengths, under which conditions type A fibrils form.[25,33] The length of lag phase was defined as the time taken to reach 10% of the maximum ThT signal at the end-point, and was estimated in a manner similar to that described by Chen *et al*.[66] Repetitions of the ThT binding experiments under equivalent agitation conditions have shown that the lag time from a given protein stock is reproducible, but different stocks can give rise to different lag times at the same concentrations of protein. Expressing times in the nucleation phase as a percentage of the total lag time allows experiments from different stocks to be compared.

### Atomic force microscopy

TM-AFM in air was performed using a Nanoscope III Multimode AFM (Veeco/Digital Instruments, Santa Barbara, CA, USA) equipped with an E-scanner (scan range up to 13 μm). Rectangular silicon cantilevers 160 μm long with resonant frequencies in the range 232–311 kHz and nominal spring constants in the range 12–103 N/m (typical 42 N/m) (Olympus, Japan) were excited slightly below the free resonant frequency, to ensure that the microscope was operating in tapping-mode. These cantilevers have integrated tips with a radius of curvature below 10 nm and a tip opening angle of 35° (Manufacturer's data, Olympus). Samples were imaged at scan sizes between 1 μm and 10 μm using line scan rates below 2 Hz and 512 × 512 pixels were collected per image. Z-piezo calibration was performed using silicon calibration grids with square-edged etch pits of 22 nm depth (NT-MDT, Russia) and 200 nm depth (Veeco).

### Sample preparation for AFM

Aliquots (10 μl) of the protein sample were deposited on mica and incubated for up to one minute, before rinsing the surface with deionised water and blow-drying with compressed nitrogen at one bar pressure (1 bar = $10^5$) and a distance of a few centimetres with the gas jet normal to the surface. The entire process of rinsing and drying took less than 30 seconds. Measurements of DNA contour lengths on mica using this sample preparation method indicate that the biomolecules are still hydrated (J. G. Heddle, A. Maxwell, N.H.T., unpublished results).

### AFM image analysis

AFM images were imported into the analysis software WSxM v2.0 (Nanotec Electronica S.L.†). To calculate the volume of aggregated protein (either amorphous aggregates or fibrils) on the mica surface or the fraction of mica surface covered by protein, the images were first flattened using a second-order plane-fit. A flooding routine was then used to calculate the image volume using a manually set threshold. The manual setting of the threshold is the most efficient way of eliminating the background from the calculated volume. Thus, the volume measured represents the volume of the aggregated protein and does not include monomeric or small oligomeric species that formed a uniform and relatively smooth layer on the mica.

The average height of fibrils above the mica was calculated using the WSxM software as follows. Images were imported and flattened using a second-order plane-fit. Fibrils of interest were isolated in software by zooming in and the flooding routine was used to determine the optimal threshold height to eliminate the background. This threshold was entered in the roughness analysis routine (a histogram of heights or bearing analysis), which returns the RMS roughness and average height of the surface. Setting a manual threshold to eliminate the background gives an average height for the selected fibril.

The peak-to-trough variations along the fibrils, the average of the maximum height of the backbone of the fibril and the average widths at half-maximal height were measured using the Nanoscope software (version 5.12r3) using the fixed axis and average options of the "Section" function.

### Electron microscopy

Colloidion-coated copper EM grids were placed coated side down onto each aliquot of $\beta_2$M and incubated for ten seconds. Excess solvent was removed by blotting with filter-paper and the sample stained with

† http://www.nanotec.es

4% (w/v) uranyl acetate for a further ten seconds. Grids were blotted again and then air-dried before analysis. All images were taken using a Jeol-1200SM electron microscope operating at 80 keV.

## Acknowledgements

We thank the BBSRC, EPSRC, the Wellcome Trust, and the University of Leeds for financial support. D.P.S. is funded by the EPSRC and S.L.M. by the BBSRC. The authors are members of the Astbury Centre for Structural Molecular Biology, which is part of the North of England Structural Biology Centre, and is funded by the BBSRC. S.E.R. is a BBSRC Professorial Fellow and N.H.T. is an EPSRC Advanced Research Fellow (AF/992774). We thank Keith Ainley for bacterial cell cultures, Adrian Hick for help with EM and the SER group for helpful discussions.

## References

1. Sipe, J. D. (1992). Amyloidosis. *Annu. Rev. Biochem.* **61**, 947–975.
2. Dobson, C. M. (1999). Protein misfolding, evolution and disease. *Trends Biochem. Sci.* **24**, 329–332.
3. Fink, A. L. (1998). Protein aggregation: folding aggregates, inclusion bodies and amyloid. *Fold. Des.* **3**, R9–R23.
4. Rochet, J. C. & Lansbury, P. T. (2000). Amyloid fibrillogenesis: themes and variations. *Curr. Opin. Struct. Biol.* **10**, 60–68.
5. Puchtler, H., Sweat, F. & Levine, M. (1962). On the binding of Congo red by amyloid. *J. Histochem. Cytochem.* **10**, 355.
6. LeVine, H. R. (1999). Quantification of β-sheet amyloid fibril structures with thioflavin T. *Methods Enzymol.* **309**, 274–284.
7. Sunde, M. & Blake, C. (1997). The structure of amyloid fibrils by electron microscopy and X-ray diffraction. *Advan. Protein Chem.* **50**, 123–159.
8. Sunde, M., Serpell, L. C., Bartlam, M., Fraser, P. E., Pepys, M. B. & Blake, C. C. F. (1997). Common core structure of amyloid fibrils by synchrotron X-ray diffraction. *J. Mol. Biol.* **273**, 729–739.
9. Harper, J. D., Lieber, C. M. & Lansbury, P. T. (1997). Atomic force microscopic imaging of seeded fibril formation and fibril branching by the Alzheimer's disease amyloid-β protein. *Chem. Biol.* **4**, 951–959.
10. Cardoso, I., Goldsbury, C. S., Muller, S. A., Olivieri, V., Wirtz, S., Damas, A. M. *et al.* (2002). Transthyretin fibrillogenesis entails the assembly of monomers: a molecular model for *in vitro* assembled transthyretin amyloid-like fibrils. *J. Mol. Biol.* **317**, 683–695.
11. Ionescu-Zanetti, C., Khurana, R., Gillespie, J. R., Petrick, J. S., Trabachino, L. C., Minert, L. J. *et al.* (1999). Monitoring the assembly of Ig light-chain amyloid fibrils by atomic force microscopy. *Proc. Natl Acad. Sci. USA*, **96**, 13175–13179.
12. Jimenez, J. L., Guijarro, J. L., Orlova, E., Zurdo, J., Dobson, C. M., Sunde, M. & Saibil, H. R. (1999). Cryo-electron microscopy structure of an SH3 amyloid fibril and model of the molecular packing. *EMBO J.* **18**, 815–821.
13. Jimenez, J. L., Nettleton, E. J., Bouchard, M., Robinson, C. V., Dobson, C. M. & Saibil, H. R. (2002). The protofilament structure of insulin amyloid fibrils. *Proc. Natl Acad. Sci. USA*, **99**, 9196–9201.
14. Goldsbury, C. S., Cooper, G. J. S., Goldie, K. N., Muller, S. A., Saafi, E. L., Gruijters, W. T. M. *et al.* (1997). Polymorphic fibrillar assembly of human amylin. *J. Struct. Biol.* **119**, 17–27.
15. Chamberlain, A. K., MacPhee, C. E., Zurdo, J., Morozova-Roche, L. A., Hill, H. A. O., Dobson, C. M. & Davis, J. J. (2000). Ultrastructural organization of amyloid fibrils by atomic force microscopy. *Biophys. J.* **79**, 3282–3293.
16. Harper, J. D., Wong, S. S., Lieber, C. M. & Lansbury, P. T. (1997). Observation of metastable Aβ amyloid protofibrils by atomic force microscopy. *Chem. Biol.* **4**, 119–125.
17. Gejyo, F., Yamada, T., Odani, S., Nakagawa, Y., Arakawa, M., Kunitomo, T. *et al.* (1985). A new form of amyloid protein associated with chronic-hemodialysis was identified as $\beta_2$-microglobulin. *Biochem. Biophys. Res. Commun.* **129**, 701–706.
18. Inoue, S., Kuroiwa, M., Ohashi, K., Hara, M. & Kisilevsky, R. (1997). Ultrastructural organization of hemodialysis-associated $\beta_2$-microglobulin amyloid fibrils. *Kidney Int.* **52**, 1543–1549.
19. Nishi, S., Ogino, S., Maruyama, Y., Honma, N., Gejyo, F., Morita, T. & Arakawa, M. (1990). Electronmicroscopic and immunohistochemical study of $\beta_2$-microglobulin-related amyloidosis. *Nephron*, **56**, 357–363.
20. Homma, N., Gejyo, F., Isemura, M. & Arakawa, M. (1989). Collagen-binding affinity of $\beta_2$-microglobulin, a preprotein of hemodialysis-associated amyloidosis. *Nephron*, **53**, 37–40.
21. Floege, J. & Ketteler, M. (2001). $\beta_2$-Microglobulin-derived amyloidosis: an update. *Kidney Int.* **59**, 164–171.
22. Floege, J. & Ehlerding, G. (1996). Beta-2-microglobulin associated amyloidosis. *Nephron*, **72**, 9–26.
23. Ono, K. & Uchino, F. (1994). Formation of amyloid-like substance from $\beta_2$-microglobulin *in vitro*. *Nephron*, **66**, 404–407.
24. Naiki, H., Hashimoto, N., Suzuki, S., Kimura, H., Nakakuki, K. & Gejyo, F. (1997). Establishment of a kinetic model of dialysis-related amyloid fibril extension *in vitro*. *Amyloid: Int. J. Expt. Clin. Invest.* **4**, 223–232.
25. McParland, V. J., Kad, N. M., Kalverda, A. P., Brown, A., Kirwin-Jones, P., Hunter, M. G. *et al.* (2000). Partially unfolded states of $\beta_2$-microglobulin and amyloid formation *in vitro*. *Biochemistry*, **39**, 8735–8746.
26. Chiti, F., De Lorenzi, E., Grossi, S., Mangione, P., Giorgetti, S., Caccialanza, G. *et al.* (2001). A partially structured species of $\beta_2$-microglobulin is significantly populated under physiological conditions and involved in fibrillogenesis. *J. Biol. Chem.* **276**, 46714–46721.
27. De Lorenzi, E., Grossi, S., Massolini, G., Giorgetti, S., Mangione, P., Andreola, A. *et al.* (2002). Capillary electrophoresis investigation of a partially unfolded conformation of $\beta_2$-microglobulin. *Electrophoresis*, **23**, 918–925.
28. Morgan, C. J., Gelfand, M., Atreya, C. & Miranker, A. D. (2001). Kidney dialysis-associated amyloidosis: a molecular role for copper in fiber formation. *J. Mol. Biol.* **309**, 339–345.
29. Esposito, G., Michelutti, R., Verdone, G., Viglino, P., Hernandez, H., Robinson, C. V. *et al.* (2000). Removal

of the N-terminal hexapeptide from human $\beta_2$-microglobulin facilitates protein aggregation and fibril formation. *Protein Sci.* **9**, 831–845.
30. Connors, L. H., Shirahama, T., Skinner, M., Fenves, A. & Cohen, A. S. (1985). *In vitro* formation of amyloid fibrils from intact $\beta_2$-microglobulin. *Biochem. Biophys. Res. Commun.* **131**, 1063–1068.
31. Saper, M. A., Bjorkman, P. J. & Wiley, D. C. (1991). Refined structure of the human histocompatibility antigen HLA-A2 at 2.6 Å resolution. *J. Mol. Biol.* **219**, 277–319.
32. McParland, V. J., Kalverda, A. P., Homans, S. & Radford, S. E. (2002). Structural properties of an amyloid precursor of $\beta_2$-microglobulin. *Nature Struct. Biol.* **9**, 326–331.
33. Kad, N. M., Thomson, N. H., Smith, D. P., Smith, D. A. & Radford, S. E. (2001). $\beta_2$-Microglobulin and its deamidated variant, N17D, form diverse amyloid fibril morphologies *in vitro*. *J. Mol. Biol.* **313**, 559–571.
34. Harper, J. D., Wong, S. S., Lieber, C. M. & Lansbury, P. T. (1999). Assembly of Aβ amyloid protofibrils: an *in vitro* model for a possible early event in Alzheimer's disease. *Biochemistry*, **38**, 8972–8980.
35. Hong, D.-P., Gozu, M., Hasegawa, K., Naiki, H. & Goto, Y. (2002). Conformation of $\beta_2$-microglobulin amyloid fibrils analyzed by reduction of the disulphide bond. *J. Biol. Chem.* **277**, 21554–21560.
36. Stine, W. B., Snyder, S. W., Ladror, U. S., Wade, W. S., Miller, M. F., Perun, T. J. *et al.* (1996). The nanometer-scale structure of amyloid-β visualized by atomic force microscopy. *J. Protein Chem.* **15**, 193–203.
37. Goldsbury, C., Kistler, J., Aebi, U., Arvinte, T. & Cooper, G. J. S. (1999). Watching amyloid fibrils grow by time-lapse atomic force microscopy. *J. Mol. Biol.* **285**, 33–39.
38. Conway, K. A., Harper, J. D. & Lansbury, P. T. (1998). Accelerated *in vitro* fibril formation by a mutant α-synuclein linked to early-onset Parkinson disease. *Nature Med.* **4**, 1318–1320.
39. Conway, K. A., Harper, J. D. & Lansbury, P. T. (2000). Fibrils formed *in vitro* from α-synuclein and two mutant forms linked to Parkinson's disease are typical amyloid. *Biochemistry*, **39**, 2552–2563.
40. DePace, A. H. & Weissman, J. S. (2002). Origins and kinetic consequences of diversity in Sup35 yeast prion fibers. *Nature Struct. Biol.* **9**, 389–396.
41. Serio, T. R., Cashikar, A. G., Kowal, A. S., Sawicki, G. J., Moslehi, J. J., Serpell, L. C. *et al.* (2000). Nucleated conformational conversion and the replication of conformational information by a prion determinant. *Science*, **289**, 1317–1321.
42. Bousset, L., Thomson, N. H., Radford, S. E. & Melki, R. (2002). The yeast prion Ure2p retains its native α-helical conformation upon assembly into protein fibrils *in vitro*. *EMBO J.* **21**, 2903–2911.
43. Kowalewski, T. & Holtzman, D. M. (1999). *In situ* atomic force microscopy study of Alzheimer's β-amyloid peptide on different substrates: new insights into mechanism of β-sheet formation. *Proc. Natl Acad. Sci. USA*, **96**, 3688–3693.
44. Blackley, H. K. L., Sanders, G. H. W., Davies, M. C., Roberts, C. J., Tendler, S. J. B. & Wilkinson, M. J. (2000). *In situ* atomic force microscopy study of β-amyloid fibrillization. *J. Mol. Biol.* **298**, 833–840.
45. Jones, S., Manning, J., Kad, N. M. & Radford, S. E. (2003). Amyloid-forming peptides from $\beta_2$-microglobulin—insights into the mechanism of fibril formation *in vitro*. *J. Mol. Biol.* **325**, 249–257.
46. Olofsson, A., Ostman, J. & Lundgren, E. (2002). Amyloid: morphology and toxicity. *Clin. Chem. Lab. Med.* **40**, 1266–1270.
47. Hou, F. F. & Owen, W. F. (2002). $\beta_2$-Microglobulin amyloidosis: role of monocytes/macrophages. *Curr. Opin. Nephrol. Hypertens.* **11**, 417–421.
48. Lomakin, A., Teplow, D. B., Kirschner, D. A. & Benedek, G. B. (1997). Kinetic theory of fibrillogenesis of amyloid-β protein. *Proc. Natl Acad. Sci. USA*, **94**, 7942–7947.
49. Lomakin, A., Chung, D. S., Benedek, G. B., Kirschner, D. A. & Teplow, D. B. (1996). On the nucleation and growth of amyloid-β protein fibrils: detection of nuclei and quantitation of rate constants. *Proc. Natl Acad. Sci. USA*, **93**, 1125–1129.
50. Poirier, M. A., Li, H., Macosko, J., Cai, S., Amzel, M. & Ross, C. A. (2002). Huntingtin spheroids and protofibrils as precursors in polyglutamine fibrilization. *J. Biol. Chem.* **277**, 41032–41037.
51. Nettleton, E. J., Tito, P., Sunde, M., Bouchard, M., Dobson, C. M. & Robinson, C. V. (2000). Characterization of the oligomeric states of insulin in self-assembly and amyloid fibril formation by mass spectrometry. *Biophys. J.* **79**, 1053–1065.
52. Khurana, R., Gillespie, J. R., Talapatra, A., Minert, L. J., Ionescu-Zanetti, C., Millett, I. & Fink, A. L. (2001). Partially folded intermediates as critical precursors of light chain amyloid fibrils and amorphous aggregates. *Biochemistry*, **40**, 3525–3535.
53. Zurdo, J., Guijarro, J. I., Jimenez, J. L., Saibil, H. R. & Dobson, C. M. (2001). Dependence on solution conditions of aggregation and amyloid formation by an SH3 domain. *J. Mol. Biol.* **311**, 325–340.
54. Ding, T. T., Lee, S.-J., Rochet, J. C. & Lansbury, P. T. (2002). Annular α-synuclein protofibrils are produced when spherical protofibrils are incubated in solution or bound to brain-derived membranes. *Biochemistry*, **41**, 10209–10217.
55. Lashuel, H. A., Petre, B. M., Wall, J., Simon, M., Nowak, R. J., Walz, T. & Lansbury, P. T. (2002). α-Synuclein, especially the Parkinson's disease-associated mutants, forms pore-like annular and tubular protofibrils. *J. Mol. Biol.* **322**, 1089–1102.
56. Hoshino, M., Katou, H., Hagihara, Y., Hasegawa, K., Naiki, H. & Goto, Y. (2002). Mapping the core of the $\beta_2$-microglobulin amyloid fibril by H/D exchange. *Nature Struct. Biol.* **9**, 332–336.
57. Kozhukh, G. V., Hagihara, Y., Kawakami, T., Hasegawa, K., Naiki, H. & Goto, Y. (2002). Investigation of a peptide responsible for amyloid fibril formation of $\beta_2$-microglobulin by achromobacter protease I. *J. Biol. Chem.* **277**, 1310–1315.
58. Zhu, M., Souillac, P., Ionescu-Zanetti, C., Carter, S. A. & Fink, A. L. (2002). Surface-catalyzed amyloid fibril formation. *J. Biol. Chem.* **277**, 50914–50922.
59. Modler, A. J., Gast, K., Lutsch, G. & Damaschun, G. (2003). Assembly of amyloid protofibrils *via* critical oligomers—a novel pathway of amyloid formation. *J. Mol. Biol.* **325**, 135–148.
60. Rhoades, E. & Gafni, A. (2003). Micelle formation by a fragment of human islet amyloid polypeptide. *Biophys. J.* **84**, 3480–3487.
61. Yong, W., Lomakin, A., Kirkitadze, M. D., Teplow, D. B., Chen, S.-H. & Benedek, G. B. (2002). Structure determination of micelle-like intermediates in amyloid protein fibril assembly by using small-angle neutron scattering. *Proc. Natl Acad. Sci. USA*, **99**, 150–154.
62. Bucciantini, M., Giannoni, E., Chiti, F., Baroni, F., Formigli, L., Zurdo, J. S. *et al.* (2002). Inherent toxicity of

aggregates implies a common mechanism for protein misfolding diseases. *Nature*, **416**, 507–511.
63. Lashuel, H. A., Hartley, D., Petre, B. M., Walz, T. & Lansbury, P. T. (2002). Neurodegenerative disease—amyloid pores from pathogenic mutations. *Nature*, **418**, 291.
64. Bitan, G., Kirkitadze, M. D., Lomakin, A., Vollers, S. S., Benedek, G. B. & Teplow, D. B. (2003). Amyloid β-protein (Aβ) assembly: Aβ 40 and Aβ 42 oligomerize through distinct pathways. *Proc. Natl Acad. Sci. USA*, **100**, 330–335.
65. Kayed, R., Head, E., Thompson, J. L., McIntire, T. M., Milton, S. C., Cotman, C. W. & Glabe, C. G. (2003). Common structure of soluble amyloid oligomers implies common mechanism of pathogenesis. *Science*, **300**, 486–489.
66. Chen, S., Ferrone, F. A. & Wetzel, R. (2002). Huntington's disease age-of-onset linked to polyglutamine aggregation nucleation. *Proc. Natl Acad. Sci. USA*, **99**, 11884–11889.

***Edited by P. T. Lansbury Jr***

*(Received 1 November 2002; received in revised form 1 May 2003; accepted 2 May 2003)*